Journal of Materials Chemistry B

Materials for biology and medicine

ROYAL SOCIETY
OF CHEMISTRY

10 YEARS ANNIVERSARY
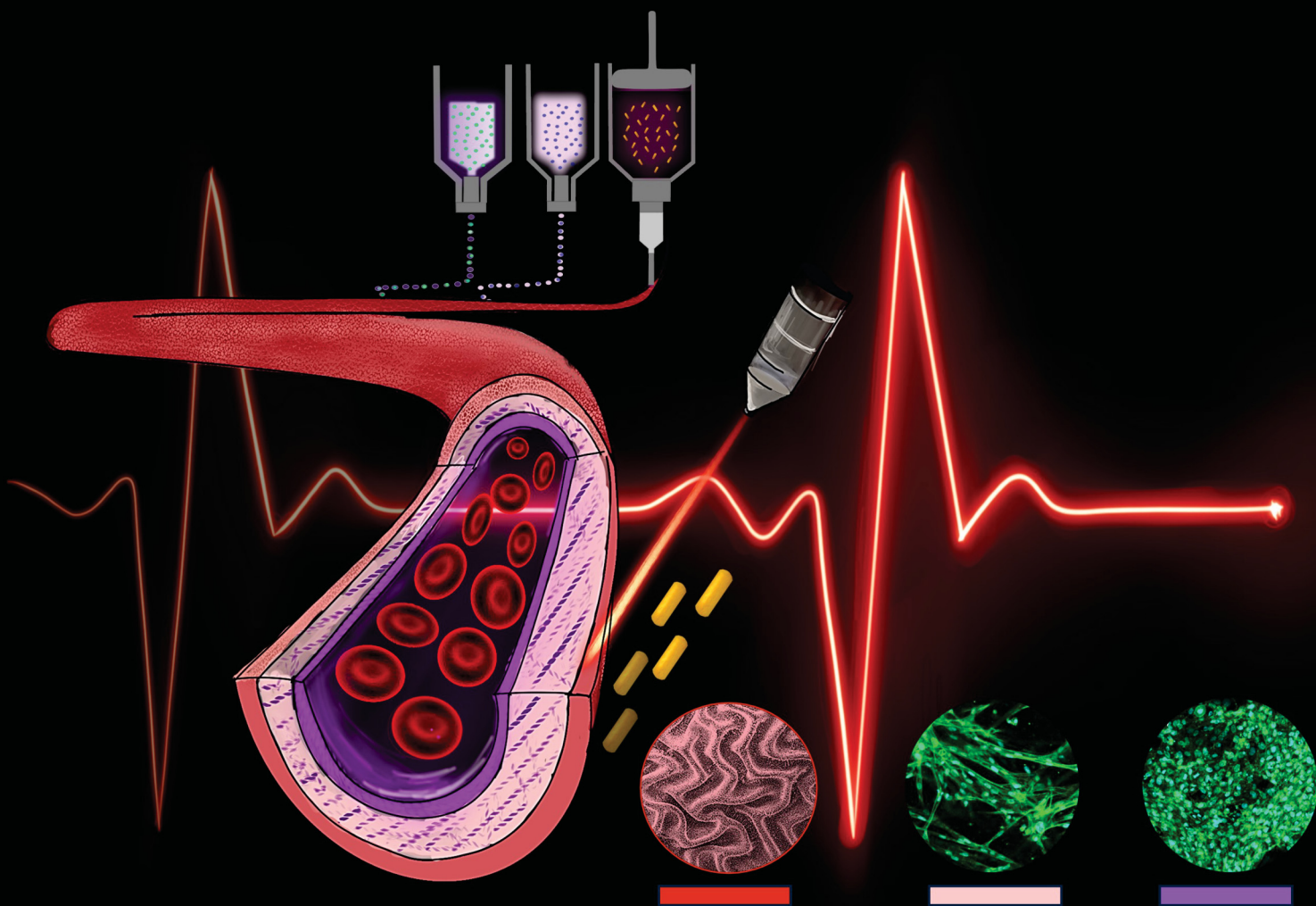
PAPER
Malou Henriksen-Lacey, Dorleta Jimenez de Aberasturi *et al*.
Remodeling arteries: studying the mechanical properties of
3D-bioprinted hybrid photoresponsive materials

PAPER

Check for updates

Remodeling arteries: studying the mechanical properties of 3D-bioprinted hybrid photoresponsive materials†

Uxue Aizarna-Lopetegui, [ID] [ab] Clara García-Astrain, [ID] [ac] Carlos Renero-Lecuna, [ID] [ac] Patricia González-Callejo, [ID] [a] Irune Villaluenga, [de] Miguel A. del Pozo, [ID] [f] Miguel Sánchez-Álvarez, [fg] Malou Henriksen-Lacey [ID] *[ac] and Dorleta Jimenez de Aberasturi [ID] *[ace]

3D-printed cell models are currently in the spotlight of medical research. Whilst significant advances have been made, there are still aspects that require attention to achieve more realistic models which faithfully represent the *in vivo* environment. In this work we describe the production of an artery model with cyclic expansive properties, capable of mimicking the different physical forces and stress factors that cells experience in physiological conditions. The artery wall components are reproduced using 3D printing of thermoresponsive polymers with inorganic nanoparticles (NPs) representing the outer tunica adventitia, smooth muscle cells embedded in extracellular matrix representing the tunica media, and finally a monolayer of endothelial cells as the tunica intima. Cyclic expansion can be induced thanks to the inclusion of photo-responsive plasmonic NPs embedded within the thermoresponsive ink composition, resulting in changes in the thermoresponsive polymer hydration state and hence volume, in a stimulated on−off manner. By changing the thermoresponsive polymer composition, the transition temperature and pulsatility can be efficiently tuned. We show the direct effect of cyclic expansion and contraction on the overlying cell layers by analyzing transcriptional changes in mechanoresponsive mesenchymal genes associated with such microenvironmental physical cues. The technique described herein involving stimuli-responsive 3D printed tissue constructs, also described as four- dimensional (4D) printing, offers a novel approach for the production of dynamic biomodels.

Introduction

Cardiopulmonary diseases (CPD) remain one of the highest causes of morbidity and mortality and hence are a huge burden to public health.[1,2] Many of the failures for lessening this burden are attributed to poor preclinical animal models which do not properly recapitulate human pathology[3,4] resulting in poor disease understanding, misidentification of risk factors,[5] and limited treatment development.[6] Thus, aside from being ethically accepted that methods to reduce animal testing *via*

implementation of the 3R's are required,[7,8] there is also a scientific need to develop novel non-animal pre-clinical *in vitro* models to better understand the tissue pathology and subsequent disease progression.

Traditionally, preclinical non-animal testing has focused on 2-dimensional (2D) cell cultures limited to single cell types (homotypic cultures) grown in monolayers. Such systems lack many of the tissue components crucial for their correct function, *e.g.* heterotypic cell mixes, growth in 3D, extracellular matrix (ECM) components, gas and liquid gradients, and

[a] CIC biomaGUNE, Basque Research and Technology Alliance (BRTA), Miramon Pasealekua, 194, 20014 Donostia-San Sebastián, Gipuzkoa, Spain.
  E-mail: mhenriksen@cicbiomagune.es, djimenezdeaberasturi@cicbiomagune.es
[b] Department of Applied Chemistry, University of the Basque Country, 20018 Donostia-San Sebastián, Gipuzkoa, Spain
[c] Centro de Investigación Biomédica en Red de Bioingeniería, Biomateriales y Nanomedicina (CIBER-BBN, ISCIII), 20014 Donostia-San Sebastián, Gipuzkoa, Spain
[d] POLYMAT, University of the Basque Country UPV/EHU, 20018 Donostia-San Sebastián, Gipuzkoa, Spain
[e] Ikerbasque, Basque Foundation for Science, 48009 Bilbao, Spain
[f] Mechanoadaptation and Caveolar Biology Laboratory, Novel Mechanisms of Atherosclerosis Program, Centro Nacional de Investigaciones Cardiovasculares (CNIC), 28029 Madrid, Spain
[g] Department of Metabolic and Immunity Diseases, Instituto de Investigaciones Biomédicas "Alberto Sols", 28029 Madrid, Spain
† Electronic supplementary information (ESI) available. See DOI: https://doi.org/10.1039/d3tb01480k

This journal is © The Royal Society of Chemistry 2023

J. Mater. Chem. B, 2023, **11**, 9431–9442 | 9431

physical stresses, among others.[4,9] The combination of modern 3D printing approaches and improved knowledge of biomaterials has opened the possibility to recreate complex 3D *in vitro* cardiopulmonary models.[10,11] Indeed, *via* the use of various 3D bioprinting techniques such as extrusion,[12] jetting,[13,14] or vat polymerization-based methods, 3D printed vessel-like structures can be successfully printed which aim to mimic various natural physiological characteristics such as size, geometry, or physicomechanical properties.[15–17] However, the exact reconstruction of the different arterial layers and the fine-tuning of the mechanical forces of the cardiovascular environment, including dynamical changes in ECM arterial wall stiffness, remain complicated to recreate.[18,19] The complexity of the arterial wall allows them to present unique mechanical features in response to physiological forces. They are constantly exposed to pressures varying between 80–120 mmHg.[20] In particular, exposure of cells to changes in substrate stiffness[21,22] or other mechanical properties can trigger important phenotypic changes and adaptive gene expression programmes, relevant to an increasing number of disorders. This process, known as mechanotransduction,[23] plays an important role in cardiopulmonary tissue, where cells are exposed to constant gas- and liquid-induced pressure changes, or flow shear forces. As with all pathologies, the distinction between a mechanism causing normal or pathological processes can be subtle. Whilst mechanotransduction is a driving force for organ development, disturbance of this homeostatic mechanism can also result in dysregulated cell proliferation, fibrosis, and phenotypic state transitions.[24] For example, endothelial-mesenchymal transition (EndoMT), by which endothelial cells (ECs) lose their characteristic tight junctions and adhesive properties, and acquire a migratory and invasive phenotype, can be induced by changes in cyclic strain.[25] In addition, the activation of specific mechanotransduction signalling pathways is associated with several inflammatory and fibrotic CPD conditions.[26–28] Moreover, pressure-induced arterial wall stress

has been associated with atherosclerosis disease.[29] Thus, recreated organotypic models should include such mechanical forces to generate realistic cell responses.[30] Indeed, 4D bioprinting which contemplates the modification of the printed 3D objects when an external stimulus is imposed,[31] has emerged as an ideal approach to reproduce such forces. Although methods to reproduce mechanotransduction have mainly focused on the application of pulsatile flow,[32] the use of thermoresponsive materials which respond in a rapid and cyclic manner can also be used to achieve pulsatility in *in vitro* models allowing a controlled change in the stiffening and stretching of the ECM. Whilst heating and cooling cycles can be achieved using heat baths or hotplates, an innovative method involves the excitation of light-sensitive plasmonic nanoparticles (NPs) embedded in thermoresponsive matrices.[33] By applying resonant light irradiation, an extremely rapid heating and cooling of the plasmonic NP surface occurs within picoseconds, with the photon energy being dissipated into the surrounding medium.[34,35] Gold NPs, and more specifically gold nanorods (AuNRs), with localized surface plasmon resonances (LSPRs) in the first biological window of the electromagnetic spectrum, are excellent candidates as nanoheaters as their anisotropy can be finely tuned to control their aspect ratio (AR) and longitudinal LSPR wavelength.[36–38] Indeed, by working in the first biological window, non-cytotoxic near-infrared (NIR) light sources which exhibit high penetrative abilities in optically transparent materials can be applied.[39,40] Whilst a variety of thermosensitive materials can be used for such applications, a crucial aspect to is the lower critical solution temperature (LCST) of the polymer, which must be of a physiological temperature for biological applications. As such, LCST modifiers can be used to raise or lower the LCST of thermosensitive polymers, without affecting their biocompatibility or miscibility. Once such example is poly (ethylene glycol) diacrylate (PEGDA), a photo-curable polymer that has good printable and optical properties for bioapplications and retains shape fidelity post-printing when crosslinked with UV light. When combined with the well-known thermosensitive polymer poly(N-isopropylacrylamide (pNIPAm) which shows a sharp phase transition at a LCST of 32 °C,[33,41] the LCST can be tuned to be closer to 37 °C.[42] Aiming to create a multi-layered structure consisting of sequentially printed cell monolayers, extrusion-based printing was used to deposit the thermoresponsive-AuNRs hybrid material allowing the obtention of well-defined structures in layered shapes or cylindrical structures. The cells, in contrast, were printed using inkjet-based printing technology that allows improved cell viability due to lower shear stress and deposition of specific volumes.

Taking these aspects into consideration, we envisaged the use of NIR light as a method to induce the rapid and cyclic expansion and contraction of an inorganic–organic matrix composed of AuNRs and the thermoresponsive copolymer pNIPAm:PEGDA, based on 4D printing technology. We applied 3D printing techniques to sequentially deposit arterial wall cells on top of the thermoresponsive material. Indeed, as hypothesized, the exposure of cells to such cyclic changes in the

Dorleta Jimenez de Aberasturi is an Ikerbasque research Fellow leading the Hybrid Biofunctional Materials group at CIC biomaGUNE (San Sebastián). She received a joint PhD between the Philipps University of Marburg (Germany) and the University of the Basque Country (Spain) in 2013, under the supervision of Prof. Teofilo Rojo, Dr. Idoia Ruiz de Larramendi, and Prof. Wolfgang Parak. She trained as a postdoc in the group of Prof. L. M. Liz-Marzán, acquiring a broad expertise in the synthesis, functionalisation, and characterisation of hybrid nanostructured materials for bioapplications. During the most recent years she has focused her interests on the biofabrication of 3D in vitro models.

Dorleta Jimenez de Aberasturi

physical properties of the underlying materials successfully induced the activation of various mechanotransduction pathways in a non-intrusive manner.

Results and discussion

Contractile artery wall model structure

The artery wall model presented herein was designed to present the following layered structure: first, a thermoresponsive material including AuNRs was deposited, followed by a layer of smooth muscle cells (SMCs) embedded in Matrigel, and finally a layer of ECs (Fig. 1). All the details related to each layer composition, 3D printing, stimuli responsiveness, and cell responses are detailed in the following sections.
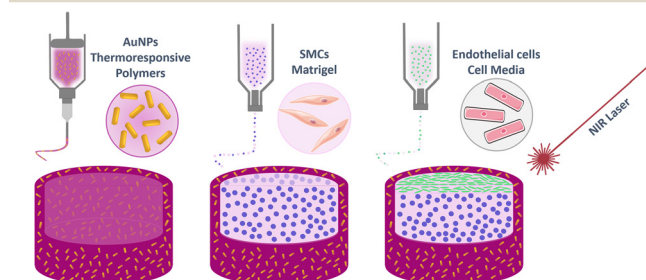
Fig. 1 Representation of the three printing steps involved in the production of the contractile artery wall model presented. From left to right: first, a thermoresponsive ink is printed forming the base and sides; secondly, SMCs are printed in ECMs; and finally, a monolayer of ECs are printed on top.

Thermoresponsive ink synthesis and characterisation

To determine the polymer formulation with optimal extrusion-based printing and thermoresponsive properties, we first studied the effect of changing the proportions of thermoresponsive ink components; pNIPAm acting as the thermoresponsive polymer, PEGDA as a photo-curable polymer, AuNRs as nanoheaters, and Pluronic 127 as a sacrificial porogen material which also acts a rheology modifier, facilitating the printability of otherwise less viscous solutions (Fig. 2A). PEGDA and NIPAm were co-polymerized under UV irradiation to shift the LCST of pNIPAm into more physiologically relevant temperatures (Fig. 2B). To study the dependence of the viscoelastic properties with temperature, focusing on a fixed PEGDA molecular weight (3400 Da), we first studied the effect of changing the weight ratio of PEGDA to NIPAm, within the temperature range at which the phase transition of pNIPAm occurs (ca. 32 °C). The storage modulus was found to slightly decrease above 35 °C (Fig. S1, ESI†), in a NIPAm:PEGDA range of 1:0.25–1:0.75, suggesting that PEGDA plays a major role regarding the temperature dependence of the modulus (Fig. S2, ESI†). The effect of PEGDA is also observed when altering the molecular weight of the PEGDA employed in the polymer formulation, with a trend of decreasing modulus as the molecular weight is increased (Fig. S3, ESI†). Although these findings suggest that low molecular weight PEGDA provides a more pronounced

rheological response to temperature in the copolymer formulation, we observed poor stability in water of 700 Da PEGDA-based hydrogels, and thus the optimal formulation was fixed at a NIPAm:PEGDA (3400 Da) ratio of 1:0.5.
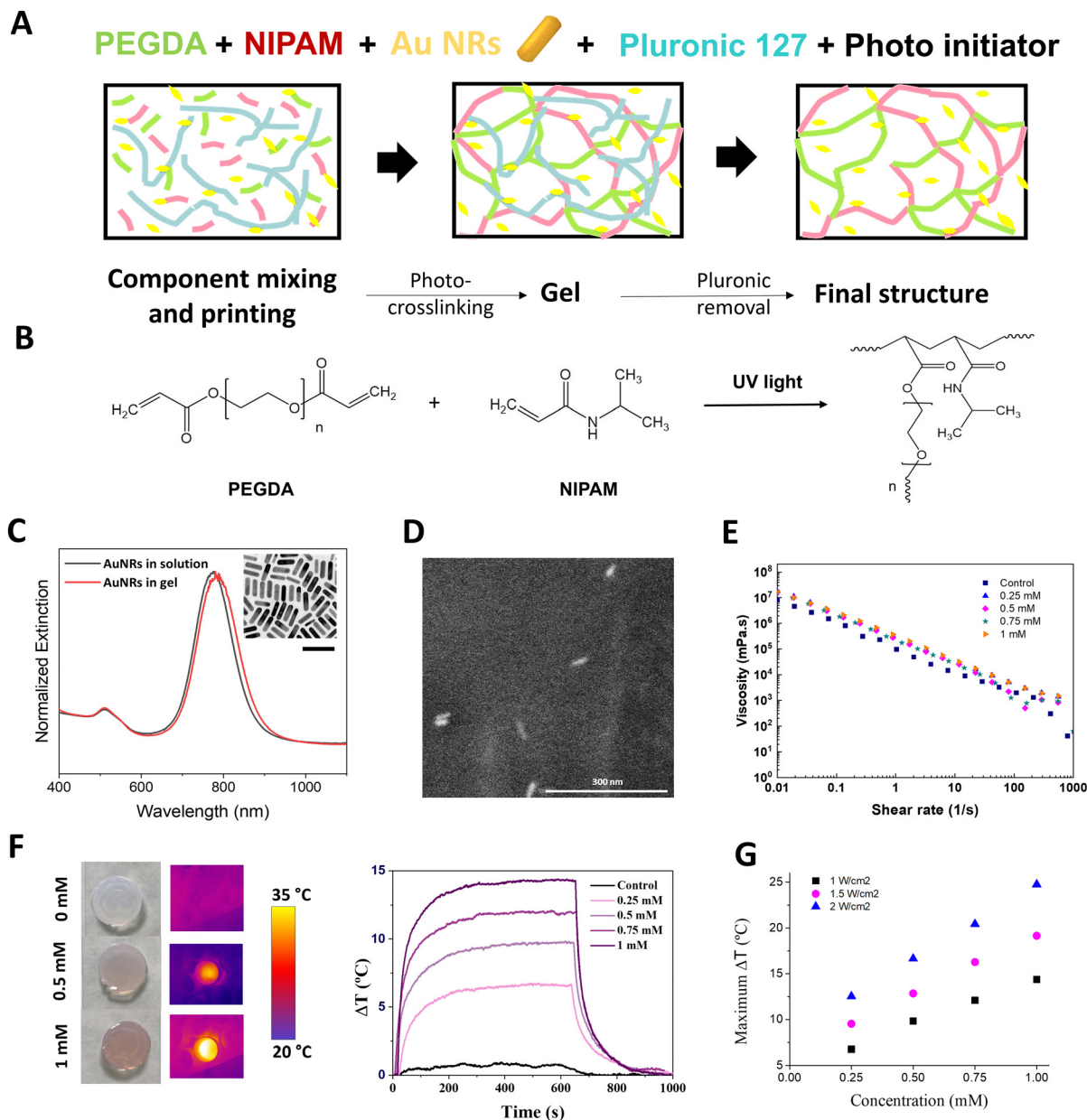
We subsequently studied the effect of AuNR incorporation on the thermosensitive and rheological properties of the inks. First, AuNRs, were characterized by UV-Vis spectroscopy, presenting a well-defined LSPR at 788 nm (longitudinal mode), and a high monodispersity with an aspect ratio of 3.6 and final dimensions of $52.6 \pm 4.9 \times 14.0 \pm 1.8$ nm, as observed by transmission electron microscopy (TEM) (Fig. 2C, inset). The inclusion of different concentrations of AuNRs (measured as $[Au^{0}]$) in the NIPAm:PEGDA formulation had no effect on the AuNRs morphology, as observed by environmental scanning electron microscopy (ESEM) and the slightly redshifted LSPR due to the higher refractive index of the gel (Fig. 2C and D). The effect of AuNRs on the LCST of the polymer mixture was characterized by differential scanning calorimetry (DSC). Whilst we observed that the inclusion and cross-linking of PEGDA with pNIPAm raised the LCST from 32 °C to 34 °C, subsequent addition of AuNRs had no significant effect on the final LCST (Fig. S4–S6 and Table S1, ESI†). Moreover, small-angle X-ray scattering (SAXS) was used to verify that no changes in the structure of the polymeric mixture occurred upon addition of AuNRs and during heating at temperatures below and above the LCST. As shown in Fig. S7 (ESI†), the absence of the peaks in the SAXS profiles indicates that all polymers presented a disordered structure. The slight increase in scattering intensity $I(q)$ observed upon addition of AuNRs are likely due to the increase of the amount of AuNR.

Rheological measurements were conducted to determine any AuNR-mediated effects on the shear-thinning and thixotropic behaviour of the inks, both important parameters for their printability. As observed in Fig. 2E, no AuNR-mediated effects on the shear thinning behaviour of the inks were observed, supporting the hypothesis that non-polymerized inks composed of AuNRs and NIPAm:PEGDA are compatible for 3D printing applications.

The recoverability of the AuNR-containing inks was studied by monitoring changes in G' while applying and removing a certain shear, simulating the printing conditions (Fig. S8B, ESI†). Although all inks showed a rapid recovery, predicting good shape fidelity of the printed structures, the recovery capacity was higher when lower concentrations of AuNRs were employed.

We proceeded next, to explore the heating behaviour of AuNR:pNIPAm:PEGDA gels, as a function of AuNR concentration. We employed an optical fiber setup with variable spot size, and real-time measurements of the local temperature were conducted by means of an infrared camera (Fig. S9, ESI†). We observed a linear relationship between temperature change and AuNR concentration, with ca. 5 min of irradiation with a continuous wave (CW) 808 nm laser, being required for the maximum temperature (T_{max}) to be reached (Fig. 2F and G). Once the laser was switched off, the gel returned to its initial temperature after ca. 5 min. These results resemble the

This journal is © The Royal Society of Chemistry 2023

J. Mater. Chem. B, 2023, **11**, 9431–9442 | **9433**

Fig. 2 (A) Schematic illustration of the components included in the thermoresponsive ink and the different steps in the synthetic process. (B) Structure of PEGDA and NIPAM and the resulting product after the polymerization process. (C) AuNR characterisation by UV-vis spectroscopy in solution (black) and in the gel (red) and TEM (inset; scale bar 100 nm). (D) Imaging of AuNRs in thermoresponsive gels *via* environmental scanning electron microscopy (ESEM). (E) Flow curves of the inks at varying shear rates. (F) Images of the gels (1 cm^2) with 0, 0.5 mM [Au^0] and 1 mM [Au^0], and their thermal characterisation under continuous wave (CW) 808 nm irradiation at 1 W cm^{-2}. (G) Maximum temperature increases as a function of AuNR concentrations using different laser powers under 808 nm laser irradiation.

behaviour of AuNRs in solution and confirm the photothermal conversion ability of AuNRs, even when immobilized in a gel. Although all AuNR concentrations tested resulted in significant changes in temperature (which could be modified by increasing laser power, see Table S2 and Fig. S10, ESI†), we fixed the final AuNR concentration at 0.5 mM based on the observation that sufficient heating could be induced with minimal loss in transparency. This is in line with previous observations relating to the decrease in surface enhanced Raman scattering (SERS) signal observed at higher AuNP concentrations.[43] The elastic

modulus of the final formulation in gel form, as opposed to liquid ink, was again measured between 25 °C and 50 °C, observing no significant differences and a typical gel behaviour at 37 °C (Fig. S11, ESI†).

In conclusion, these findings confirm the thermosensitive and stable nature of hybrid AuNR-containing pNIPAm:PEGDA gel, and that exposure to temperatures between 30 and 40 °C has no irreversible effect on the polymer morphology, thus supporting its suitability for the intended pulsed heating application.

Cyclic heating

The macroscale properties of the thermoresponsive gel were studied, focusing on their porosity. Moreover, the cyclic nature of contraction and expansion of the gels was explored. Using a hot-plate heating setup, significant contraction was observed upon heating the thermoresponsive gel above its LCST (Fig. 3A). Indeed, when self-standing 8 cm tall cylinders were printed, a *ca.* 50% decrease in height was observed above 37 °C. Cyclic swelling studies conducted in aqueous media showed a similar trend; reproducible cycles of expansion and contraction were observed when varying the temperature between 32 °C and 37 °C (Fig. 3B). This behaviour is consistent with the transitioning from hydrophilic to hydrophobic state above the LCST of pNIPAm-based hydrogels, subsequently resulting in expulsion of water and subsequent gel contraction. SEM imaging was used to observe the changes that occurred in the overall microstructure and porosity of the expanded and contracted states. The porosity of the gels is a result of the inclusion of the sacrificial polymer Pluronic 127, removed post printing by extensive washing at 4 °C (Fig. S12, ESI†). When the gels were heated above their LCST, macroscale ripples with small pores were observed. In contrast, at temperatures below their LCST, smoother ripples with significantly larger pores were observed. As can be appreciated, the expanded and contracted states result in impressive differences in the porosity and surface

morphology (Fig. 3C). In its contracted form, the surface shows folds measuring *ca.* 100 μm from crest to crest, and pores measuring <5 μm in diameter.

We next studied the *in situ* heating ability of the AuNRs embedded in the thermoresponsive gel. We have previously shown that AuNRs of similar size and aspect ratio can effectively convert incident NIR light irradiation into heat using a similar optical fiber laser setup.[44] Furthermore, both continuous and pulsed laser cycles can be applied, providing flexibility to the system design. Thus, we proceeded to optimise the laser-heating experimental design to achieve rapid and cyclic heating that can simulate the pulsatility of human arteries (for full details, see Methods section). Using a continuous irradiation laser setup (808 nm wavelength), we first observed that the higher maximum temperatures (T_{max}) could be reached with increasing laser power densities (1–3 W cm^{-2}) (Table S3, ESI†). In a similar way, increasing pulsed laser density power at 808 nm wavelength and/or AuNR concentration also resulted in increased T_{max} (Table S4 and Fig. S13, ESI†). Considering that we aimed at a cyclic expansion and contraction of the gel, we optimized the illumination time, finally selecting an on/off cycle of 4 s/16 s which allowed us to maintain the maximum and minimum temperatures within the range of the LCST (Fig. S14, ESI†). Additionally, we investigated the importance of the starting temperature, controlled by placing the sample
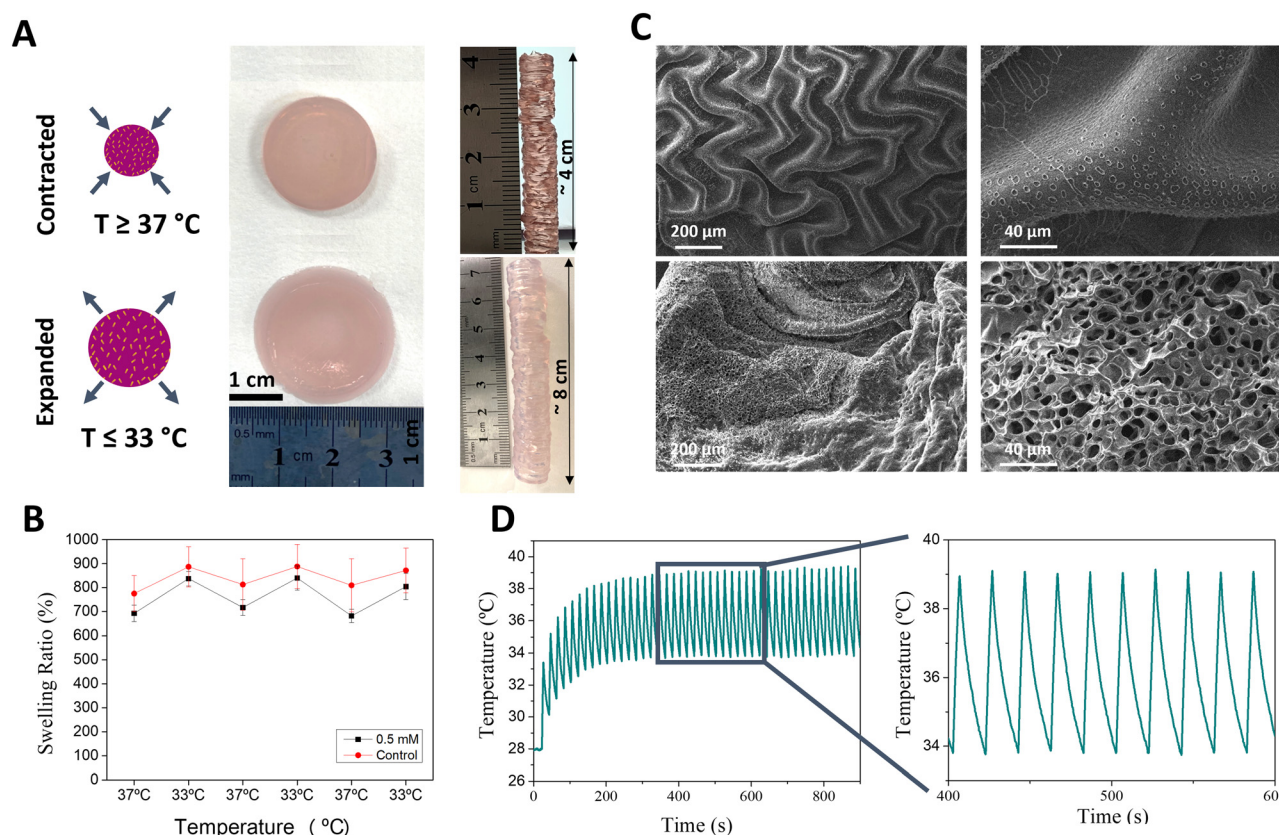

Fig. 3 (A) Photographs of expanded and contracted cylindrical and tube-shaped gels when heated above (contracted) and below (expanded) the LCST. (B) Swelling test of the gels at 37 and 33 °C. (C) SEM characterisation of contracted, top, and expanded, down, gels. (D) Pulsed illumination of the 3D printed AuNR − thermoresponsive gel with the heating plate set to 31 °C and laser density power of 2.5 W cm^{-2}.

This journal is © The Royal Society of Chemistry 2023

J. Mater. Chem. B, 2023, **11**, 9431–9442 | **9435**

on a hot plate. As can be observed in Fig. S15 (ESI†), T_{max} was directly proportional to the starting temperature. Therefore, the optimal heating setup involved pulsed (4s on/16s off) irradiation (2.5 W cm^{-2}) of gels maintained at a baseline temperature of 28–30 °C using a heat-plate (Fig. 3D). The cyclic heating process was reproducible over time, suggesting that the system remains stable. Indeed, we observed that the absorbance spectra of the gels did not change significantly after heating (Fig. S16, ESI†), indicating negligible AuNR reshaping and thus confirming the non-invasive character of this technique during hydrogel expansion and contraction.

We subsequently proceeded to measure the contraction and expansion capacity of our gels. We bioprinted cylinders measuring 6 mm in [external] diameter, thus mimicking the dimensions of a medium human artery.[20,45] The cylinders were heated under the previously established conditions, and videos of 20 min duration were recorded. The videos were segmented in 5 s fragments and converted into images (see Experimental section). By analysing the area of the cylinder and the internal lumen during the pulsed irradiation, we concluded that the material is able to contract by *ca.* 1.5 mm (equivalent to a 25% reduction in diameter) during each heating cycle (Fig. S17, ESI†), in agreement with reported literature values describing the extent of physical change required to induce cellular mechanotransduction.[46]

3D printing of the pulmonary artery wall model

Having demonstrated that the selected material responds to external laser stimulation, inducing the expansion and contraction of the gel, the 3D tissue model was finally built up. We studied the ability of the thermoresponsive gel to mimic the native contractile nature of the pulmonary artery in an *in vitro* model consisting of 3D-printed SMCs and ECs. For this study, we designed a layered model, as opposed to concentric circles, to ensure better control of cell deposition. A ''Cell Friendly'' (RegenHU) printhead was used for both cell types with an electronically controlled microvalve to allow deposition of cells in liquid and low viscosity fluids (see Experimental section).[47] We chose the commercial extracellular matrix Matrigel as the 3D matrix for SMC printing. In contrast, ECs were printed in liquid state without any 3D matrix. Neither printing technique was found to have any effect on EC or SMC cell viability and morphology, as confirmed by their cell densities and morphologies (Fig. S18, ESI† and Fig. 4A), where elongated cells pre- and post- printing can be observed. We verified the non-toxic nature of our AuNR-containing thermoresponsive gels by exposing cells to media in which thermoresponsive gels had been incubated for various periods of time. As shown in Fig. S19 (ESI†), cytotoxicity lower than 5% was observed after incubation of gels with media for ≤5 days. We verified the time-dependent stability of the gels by conducting Inductively coupled plasma mass spectrometry (ICP-MS) measurements at the same time-points. Less than 1% of the AuNRs were observed to leach from the gels over a 5-day period (Table S5, ESI†). Thus, we demonstrated that AuNRs remain embedded in the polymeric matrix, and that the hybrid mixture was not cytotoxic. We printed 6 mm^2 squares of thermoresponsive gel in microscopy imaging μ-slides with 10 mm^2 wells (Fig. S20, ESI†). Of note, printed gels were considerably smaller than the well itself to allow for expansion of the gel during the Pluronic 127 removal washing step, as well as for size changes occurring during cyclic stimulation. In addition, a 5-layer high wall was printed on top of the
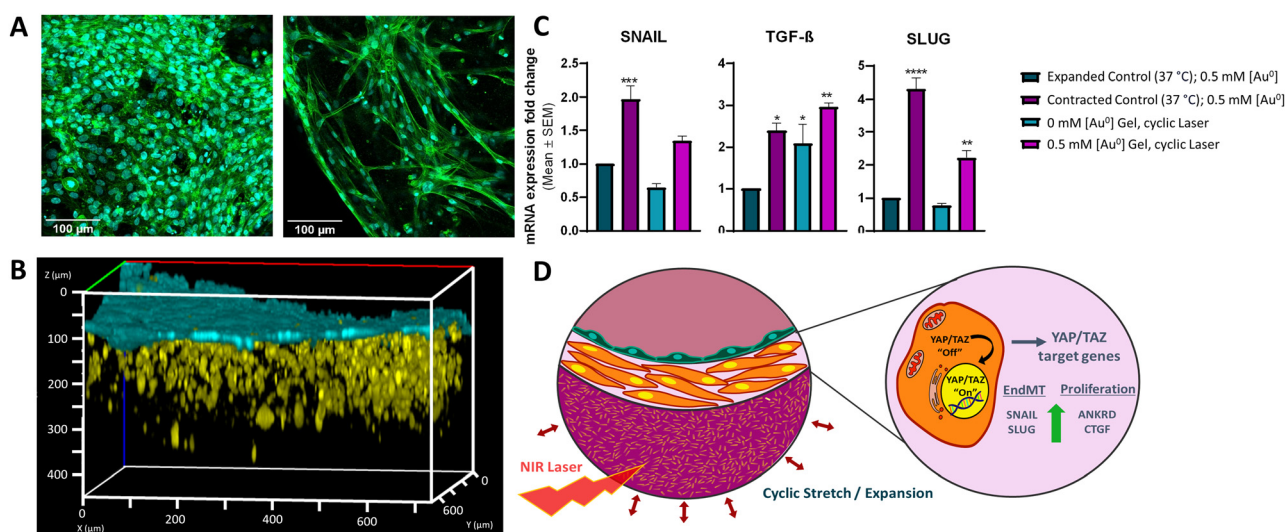
Fig. 4 3D printed artery model. (A) Actin and DAPI staining of the ECs monolayer (left) and SMCs embedded in Matrigel (right). (B) 3D rendition of live cell fluorescence confocal images showing SMCs (yellow) embedded in Matrigel and ECs (blue). (C) qRT-PCR analysis of SNAIL, TGF-β, and SLUG expression in SMCs and ECs recovered from models exposed to different conditions including AuNR (0.5 mM [Au^0]) containing gels incubated at 33 °C (green) and 37 °C (purple), and the gels (both control gel (no AuNRs: 0 mM [Au^0] (blue) and AuNR (0.5 mM [Au^0] (fuchsia)) containing gel) exposed to cyclic laser irradiation (2.5 W cm^{-2}, 4 s on/16 s off) for 4 h. Data shows mean +/− SEM with significance differences (one-way ANOVA followed by Dunnett's multiple comparisons test) tested against expanded control (*$P ≤ 0.05$, **$P ≤ 0.01$, ***$P ≤ 0.001$, ****$P ≤ 0.0001$). (D) Schematic representation of the cellular response upon the external stimulation *via* NIR laser irradiation.

square thermoresponsive gel to retain the subsequently printed cell-containing inks. Indeed, in initial trials without this outer wall, we observed that the controlled deposition of Matrigel embedded cells and subsequent endothelial cells could not be achieved without them falling off the thermoresponsive gel and adhering to the underlying μ-slide surface. Additionally, the degree of hydration of the underlying thermoresponsive gel layer was crucial to allow attachment of Matrigel-embedded SMCs; various studies have described the importance of substrate characteristics for optimum Matrigel-substrate interactions and subsequent SMC contractile forces in response to Matrigel signalling cues.[47–49] In this regard, special care was taken to remove as much of the Pluronic 127 washing solution prior to printing Matrigel, thus promoting the strongest possible interactions between the thermoresponsive gel and Matrigel (Fig. S21, ESI†). In order to have a better understanding of the cell distribution and morphology in 3D, we characterized the printing of both cell layers using fluorescence confocal microscopy (Fig. 4B and Fig. S22A, ESI†). As can be observed, SMC distribution in Matrigel was homogenous, forming a layer *ca.* 200 μm thick, with a thin (≤50 μm) layer of ECs above. Considering that we could not observe the underlying thermoresponsive material by confocal microscopy, we conducted SEM imaging to determine the interaction between both layers (Fig. S22B, ESI†). Although both cell populations could be distinguished, based on cell morphology (false coloured for clarity in the figure), the thickness and distribution did not match with that observed *via* confocal microscopy. We propose that this is due to the invasive fixation and drying process for SEM analysis.

Finally, we studied the effect that repetitive contraction-expansion of the thermoresponsive layer, induced by laser irradiation, could triggers on the cells. Specific mechanical cues, such as cyclic strain and substrate stiffness, can promote mesenchymal phenotype activation signatures.[50–52] Furthermore, cells of mesenchymal lineage such as SMCs and fibroblasts can also upregulate these gene sets in response to mechanical stimuli, as many of them are functionally involved in cell-ECM reciprocal crosstalk and biomechanical ECM remodeling. We exposed our model to pulsed laser irradiation using the same conditions described earlier (2.5 W cm^{-2}, 4 s on/16 s off). This on/off cycle was repeated during 4 h, followed by the subsequent recovery of the cells using commercial cell recovery solution. Harvested cells were analyzed by qRT-PCR to assess the expression levels of genes associated with the yes-associated protein (YAP)/transcriptional coactivator with PDZ-binding motif (TAZ) mechanotransduction pathway, crucial in relaying mechanical and physical cues from the ECM to dictate subsequent cell behaviour.[27] Specifically, we investigated the gene expression profiles of mesenchymal markers including SNAIL, TGF-β, and SLUG, as well as canonical YAP/TAZ target genes ANKRD1 and CTGF.[22,53] We observed upregulation of all genes in cells growing in gels at 37 °C in a contracted state compared to the cells growing in the gel presenting an expanded state at 33 °C (Fig. 4C and Fig. S23, ESI†). Remarkably, this upregulation was also observed in cells isolated from the models

containing NRs that had been exposed to laser irradiation, thus simulating cyclic strain and therefore, showing cyclic gel contraction and expansion, and thus mechanical stress. No significant changes were observed in cells recovered from control models without NRs yet exposed to laser irradiation (gels existing in a continuously expanded state). These observations support our 3D printed artery model as a system that can recapitulate physiological responses of printed cells to controlled mechanical stimuli, mimicking substrate stiffening from ECM remodeling and pulse wave-derived stretching, as occurs *in vivo*.

Conclusions

More complex *in vitro* models such as 3D cell culture models are increasingly taking importance, where 3D printing is starting to be a key player in the fabrication of such native tissue replicas. 3D printing presents many possibilities and advantages in medicine, but as is a relative new field there is still much work to do, to produce effective materials which are printable, stable, with improved mechanical properties, and which respond to desired stimuli. With this regard, we have focused on the development of printable hybrid smart bioinks that can respond to external stimuli for the reproduction of the forces that occur in pulmonary arteries. The results obtained so far suggest the suitability of using 3D printing for the generation of 3D tissue models based on such smart-hybrid living bioinks. Both the developed stimuli-responsive inks containing AuNPs and living bioinks containing representative cells, present appropriate rheological properties for printing together with highly porous structures, facilitating the diffusion of nutrients, oxygen and heat throughout the whole system. More specifically, the introduction of nanoparticles within polymeric networks provides the system with multifunctionality together with stimuli-responsiveness, where the AuNPs when irradiated with a NIR laser causing the subsequent increase in the local temperature. The heating parameters have been optimized to generate the expansion and contraction of the material upon laser illumination, mimicking the pulsatility of arteries. The living bioink is biocompatible and provides an environment constructive for the growth of different cell types both embedded within it and printed on top. Through 3D bioprinting we have been able to arrange the cell of interest, that compose the native tissues into multi-layered systems, representing the different layers found in arteries.

Interestingly, we have shown that the NIR-induced pulsed irradiation leading to thermoresponsive gel contraction induces the expression of mesenchymal activation gene signatures associated with the YAP/TAZ pathway, which is a central mechanotransduction network (Fig. 4D). Our data unveils that our model not only resembles physiological artery contractions but also confirms that this mechanical stress due to cyclic strain provokes changes in substrate stiffness that can be sensed by SMCs and ECs, mimicking their behaviour in their physiological environment. Additionally, we show that

This journal is © The Royal Society of Chemistry 2023

J. Mater. Chem. B, 2023, **11**, 9431–9442 | **9437**

the incorporation of stimuli-responsive plasmonic NPs into thermoresponsive matrixes allows the recreation of different mechanical forces, opening new avenues for much-needed *in vitro* modelling. This novel approach to induce pulsatile effects for the fabrication of artery models allows the fabrication of suitable platforms to achieve a deeper understanding of the molecular and cellular mechanisms underlying different CPDs, in addition to providing a realistic alternative to traditional *in vitro* and *in vivo* models used to investigate therapeutic opportunities. It should be noted that there is wide variation in the geometric and physico-mechanical properties of arteries depending on the species, tissue, and health status of the artery in question. In future studies we will fabricate 3D layered cylindric structures aiming to recreate the compliance and pressures that arteries are exposed to mimicking native human arteries.

Experimental section

Materials

Hexadecyltrimethylammonium bromide (CTAB, $\geq$99.0%), 5-bromosalicylic acid (5-BrSA, technical grade, 90%), hydrogen tetrachloroaurate trihydrate (HAuCl$_4$·3H$_2$O, $\geq$99.9%), silver nitrate (AgNO$_3$, $\geq$99.9%), L-ascorbic acid (AA, $\geq$99%), sodium borohydride (NaBH$_4$, 99%), N-isopropylacrylamide (NIPAm, 97%), poly(ethylene glycol) diacrylate (PEGDA, Mn 250 and 700), Pluronic® F-127, 2-hydroxy-4'-(2-hydroxyethoxy)2-methyl-propiophenone) (Irgacure 2559, 98%), ammonium persulfate (APS, $\geq$99.0%), N,N'-methylenebis(acrylamide) (BIS, 99%), N,N,N',N'-tetramethylethylenediamine (TEMED, ~99%), hexamethyldisilazane (HDMS), were all purchased from Sigma Aldrich. Poly(ethylene glycol) diacrylate (PEGDA, Mn 3400 and 8000), paraformaldehyde (PFA), trypsin-EDTA, penicillin–streptomycin (PS), Cell Tracker probes, DAPI, actin-488 ReadyProbes, lactate dehydrogenase (LDH) kit, and High Capacity cDNA Reverse Transcription Kit were all purchased from Thermo Fisher Scientific. Human Pulmonary Artery Smooth Muscle Cells (SMCs, ATCC-PCS-100-023), Human Aortic Endothelial Cells (TeloHAEC, ATCC CRL-4052), Vascular Cell Basal Media (ATCC-PCS-100-030), Vascular Endothelial Cell growth supplements (ATCC PCS-100-041), and Vascular Smooth Muscle Cell growth supplements (ATCC-PCS-100-023) were purchased from ATCC. Matrigel and Matrigel cell recovery solution were purchased from Corning. High-walled 8-well Ibitreat microslides were purchased from Ibidi. iTaqTM Universal SYBR Green Supermix was purchased from BioRad and the RNeasy Mini Kit from Qiagen. Osmium tetraoxide (OsO$_4$) and glutareldehyde were purchased from Electron Microscopy Services (EMS). All chemicals were used as received. Milli-Q water was used in all experiments. All glassware used for AuNRs synthesis was washed with aqua regia, rinsed with water and dried before use.

Instrumentation

UV-Vis spectroscopy was carried out using an Aligent 8453 diode-array spectrophotometer. Differential Scanning Calorimetry (DSC) analysis was conducted using a Mettler Toledo model. Transmission Electron Microscopy (TEM) were collected with a JEOL JEM-1400PLUS operating at an acceleration voltage of 120 kV. Rheological properties were characterized using a controlled stress MCR 302 rheometer (Anton Paar) with a custom 25 mm parallel-plate geometry with laser etched surface, to avoid wall slip, at 25 °C and with a water solvent trap to prevent sample evaporation and ensure a saturated atmosphere.[54] A JEOL JSM-6490LV Scanning Electron Microscopy (SEM) working at an acceleration voltage of 5–15 kV was employed for SEM imaging. Wet thermoresponsive gels were imaged using Environmental Scanning Electron Microscopy (ESEM-FEI QUANTA 250) working at an acceleration voltage of 30 kV, under a pressure of 70 Pa. Confocal fluorescence imaging was conducted using a Zeiss LSM 880 microscope equipped with argon, DPSS and HeNE lasers. For heating experiments, a homemade setup (Fig. S19, ESI†) consisting of a diode fiber-coupled 808 nm laser (Lumics, LuOcean mini8, LU0808D105), a near infrared camara (FLIR AX35), a Heidolph heating plate and a portable microscope (Aven, Mighty Scope 1.3 M, 175×), was built. 3D printing was performed using a multi-headed 3D Discovery bioprinter (RegenHU, Switzerland). The bioprinter is equipped with various print heads that use different printing mechanisms. A high precision plunger dispenser was used for extrusion printing. Cells were inkjet printed using a "Cell Friendly" (2C-PH) printhead with an electronically controlled microvalve to allow deposition of cells in liquid and low viscosity fluids. The core part of the valve is composed a ruby valve ball that allow precise opening strokes of a few hundreds of a millimetre ensuring high accuracy in volumetric printing. The opening-close speed can be controlled to adjust the jetted volumes.

Thermo-responsive polymer design and characterisation

Gold nanoparticle synthesis and characterisation. Gold nanorods (AuNRs) were synthesized using a previously established protocol.[38,55] To produce Au seeds, 25 µl of a 50 mM HAuCl$_4$ solution was added to 4.7 mL of 0.1 M CTAB solution which was stirred for 50 min before adding, under vigorous stirring, 300 µl of a freshly prepared 10 mM NaBH$_4$ solution at 30 °C to produce the seeds, which were subsequently kept at room temperature (RT) for 30 min for the consumption of the borohydride excess. Aside, 45 mg of 5-BrSA were added to 25 mL of 0.1 M CTAB. Once completely dissolved, 480 µl of 0.01 M AgNO$_3$ was injected and the mixture was stirred at RT for 15 min. The process was followed by the pre-reduction of Au(III) to Au(I) for which 500 µl of 50 mM HAuCl$_4$ solution were added to the solution and left until an absorbance of 0.8–0.85 was observed at 396 nm by UV-vis spectroscopy, corresponding to the longitudinal plasmon band at 800 nm. Subsequently 130 µl of 100 mM AA was added and after 30 s, 80 µl of the seeds were injected under vigorous stirring for 30 s, after which the stirring was stopped and the resulting AuNRs left undisturbed for 4 h. The mixture was then purified by centrifugation, twice at 8000 rpm for 20 min at 25 °C. This method resulted in AuNRs with a max absorbance at 788 nm. AuNR characterisation *via*

9438 | *J. Mater. Chem. B*, 2023, **11**, 9431–9442

This journal is © The Royal Society of Chemistry 2023

TEM was conducted by drop casting on a carbon-coated 400 square mesh Cu grid.

Polymeric ink development. Based on previous work described by Son *et al.*,[42] different ink compositions were prepared by varying the concentration and ratios of PEGDA and NIPAm. Specifically, four different PEGDA molecular weights (250, 700, 3500 and 8000 Da) were explored, combined at three different weight ratios (4, 8 and 12 wt%) with NIPAm (16 wt%). A control formulation containing 8 wt% PEGDA (3400 Da) without NIPAm was also prepared. Irgacure (0.5 wt%) was used as the initiator to photopolymerize the NIPAm with PEGDA. Additionally, a 16 wt% NIPAm gel was prepared in presence of APS (0.1 g ml^{-1}), BIS (25 mg ml^{-1}) and TEMED (0.1 v/v%) as a control sample without PEGDA. All reagents were dissolved in distilled water under continuous stirring at RT. Once the mixture was completely homogeneous, Pluronic F127 (21.5 wt%) was added and the solution stirred in an ice bath until complete dissolution.

For inks containing AuNRs, AuNRs were carefully washed (9000 rpm, 20 min) to remove excess CTAB, followed by resuspension in H$_2$O to a final concentration of at least 5 mM. AuNRs were added to the polymer inks to achieve final concentrations of 0.25, 0.5, 0.75 or 1 mM AuNR, always respecting the previously described final polymeric weight ratios. The samples were mixed under vigorous stirring in an ice bath until the nanoparticle suspension was homogenised in the ink, followed by mixing using a Thinky Mixer at 3500 rpm for 5 min. Samples were stored at 4 °C before usage.

Rheology. Amplitude sweeps from 0.001 to 100% strain, at a constant angular frequency of 1 Hz, were performed to determine the linear viscoelastic region for each composition of non-polymerized ink and gel (Fig. S8A and S11A, ESI†). Additionally, steady shear flow and viscosity curves were measured by performing shear rate sweeps from 0.01 to 1000 s^{-1}. Finally, thixotropy measurements replicating the printing process were performed to characterize the material's recovery behaviour, by subjecting the material to a 3-step test, starting with monitoring the material at rest for 120 s at 0.01% strain and 1 Hz, followed by a shear rate of constant shear rate of 700 s^{-1} (estimated from the power law model for non-Newtonian fluids) for 120 s, and finally measuring the recovery of the material at rest for 400 s (Fig. S8B, ESI†). To test the rheological properties of the final cross-linked hydrogels, hydrogel discs of 25 mm of diameter were prepared. To determine the storage and loss moduli of the different samples, frequency sweeps were carried out from 500 to 0.1 rad s^{-1}, at a fixed strain within the viscoelastic region. Temperature ramps were performed from 20 to 50 °C and from 50 to 20 °C at 1 °C min^{-1} at 1 Hz and 0.01% strain.

Swelling study. A general gravimetric method was employed for testing the swelling capacity of the hydrogels. Hydrogels with and without AuNRs (0.5 mM) were freeze-dried for 72 h followed by incubation at 33 °C or 37 °C in vascular cell culture media. At selected time intervals swollen gels were weighted, removing the excess media with filter paper. The swelling ratio

(SR) was calculated using the following equation:

$$SR = \frac{(W_s - W_d)}{W_d} \times 100$$

where W_s is the weight of the swollen sample and W_d is the weight of the dried gel sample.

Additionally, to verify that AuNRs did not leach from the swollen gels, ICP-MS was performed at various timepoints. Specifically, 9 mm hydrogel disks were incubated in cell media at 33 °C and 50 μl media collected after 1, 2 and 5 days. Samples were diluted in 450 μl aqua regia to digest any possible AuNRs, prior to ICP-MS measurements.

Heating experimental design. To characterize the transition temperature of the hydrogel and verify the increase of the LCST of NIPAm due to the incorporation of PEGDA, DSC was performed. A dynamic sweep from 10–70 °C was performed at 5 °C min^{-1} in a nitrogen atmosphere. The samples analysed included the hydrogel compositions of 16 wt% NIPAm combined with 8 wt% PEGDA of 3400 or 8000 Da, resulting in a 1:0.5 polymeric ratio, in addition to a 1:0.75 polymeric ratio (12 wt% NIPAm with 8 wt% PEGDA) using 3400 Da PEGDA. In the case of the 1:0.5 NIPAm:PEGDA (3400 Da) sample, the contribution of the incorporation of AuNRs (0.5 and 1 mM) was also studied. In total five different formulations were evaluated using DSC. The LCSTs of each of the hydrogel formulations was determined as the average of the inflection points of the second and third plot of the temperature change profiles of the DSC curves. The first sweeps, including both the heating and the cooling ramps, were discarded in all cases to ensure the stabilisation of the system and erase the previous thermal history of the material.

To homogenously irradiate the AuNR-containing solutions and hydrogels, an 808 nm laser with a beam size of 9 mm diameter was employed and the temperature change profiles were recorded by the NIR camera at a rate of 30 Hz. Hydrogel discs, measuring 9 mm in diameter to ensure that the whole sample was irradiated, were placed in high-walled 8-well microslides and 300 μl of cell media added. The microslide, without lid, was placed on a hot plate set to 31 or 35 °C; special care was taken to verify that the heat plate had a homogenous heat pattern. With the aim of obtaining further information of the effect of the external stimulation upon NIR irradiation on the gels, the portable microscope was used to record the heating process. Finally, when irradiating the 3D printed cell-containing models, a calcium fluoride (CaF$_2$) slide was employed to maintain sterility whilst allowing IR-camera measurements.

SAXS. The samples were prepared and measured in glass capillary tubes. SAXS data was collected on the BL11-NCD beamline at ALBA (Barcelona, Spain). The X-ray wavelength used was 0.99 Å, with a sample-to-detector distance of 2.9 m for the SAXS. In the present paper, the scattering curves are plotted as a function of the scattering vector q defined as $q = 4p/l \cdot \sin(q/2)$ with q the scattering angle. Standard data corrections were applied.

This journal is © The Royal Society of Chemistry 2023

J. Mater. Chem. B, 2023, **11**, 9431–9442 | **9439**

Image processing for the expansion and contraction analysis. The expansion and contraction of the irradiated 3D printed cylinders was assessed by segmenting the cylinder and measuring the difference in the total area (number of pixels within the segmented region multiplied by pixel's area) in both states. The irradiation of the cylinders by the laser was recorded by portable microscope (Aven, Mighty Scope 1.3 M, 175×) and the videos (ESI,† Video 1, pulsed irradiation and Video 2 continuous irradiation) were converted to images (15 images per second) using the FFmpeg software (Available at https://ffmpeg.org). The resulting RGB images were transformed to 8-bit images, binarized using an optimized threshold and subjected to processing steps such as erosion and dilatation (see Fig. S17, ESI†). The segmentation was performed using fslmaths, fslsplit[56] and c3d[57] programs and visualized in ITK-SNAP.[58,59] Finally, the data was analysed in Matlab.

Development of the multi-layered *in vitro* model

Cell culture. Human artery endothelial cells (TeloHAEC) and Human Pulmonary Artery Smooth Muscle Cells (SMCs) were cultured in Vascular Cell Basal Media supplemented with vascular endothelial cell and vascular smooth muscle growth supplements, respectively. TeloHAEC were used between passages 2 and 10; SMCs were used between passages 2 and 6. Both TeloHAEC and SMCs were trypsinized using $0.5\times$ trypsin-EDTA. For fluorescence imaging, TeloHAECs were labelled with CellTracker Blue and SMCs in CellTracker Deep Red, both in vascular cell basal media, at a final concentration of 100 μM and 4 μM, respectively.

Bioink preparation. Two cell containing formulations were used as the biological components of the system. Working on ice, CellTracker stained SMCs (6×10^6 cells per ml) were mixed with Matrigel at a 1 : 1 volume ratio to form the SMC bioink. In addition, TeloHAECs were prepared at 1.5×10^7 cells per ml to produce the overlying endothelial cell layer.

Elemental and microscopical characterisation. SEM of the thermoresponsive and cell-containing bioinks was performed to determine the microstructure of the printed constructs, in addition to the spatial distribution of the nanoparticles within the polymeric matrix. Samples composed of the thermoresponsive layer without cell bioinks were quenched in liquid nitrogen in their expanded and contracted states to characterize the structural differences occurring. For SEM imaging of the cell-containing multi-layered constructs, samples were first incubated for 2 h at RT in a fixation solution of glutaraldehyde (2.5%) and formaldehyde (2%), prepared in a 0.1 M solution of sucrose in Sorensen's buffer. Samples were washed ($3\times$) in Sorensen's buffer and subsequently exposed to OsO$_4$ (1% in Sorensen's buffer), for 1 h on ice. Again, the samples were washed ($3\times$), followed by an ethanol dehydration series consisting of 30, 50, 70, and anhydrous 100% ethanol (the latter performed three times). Finally, the samples were submerged in HDMS which was allowed to slowly evaporate, before mounting samples on SEM stubs for imaging.

3D printing. Different bioprinting strategies were explored to create a multi-layered structure consisting of sequentially printed cell monolayers. The G-code for printing the structures

was produced using BIOCAD software (RegenHU, Switzerland). Both extrusion and inkjet-based printing approaches were tested for the precise deposition of bioink formulations of different viscosities. The printing conditions, including the printing pressure and feed rate, cartridge temperature, number and height of layers and their initial height, printing design, and needle tip diameter were all optimized for each material composition (see Tables S6 and S7, ESI†). The initial printing height was established based on the support and height of the base in which it is being printed over. The highly viscous thermoresponsive ink formulation was printed using a high precision plunger dispenser at a constant volume flow rate of 2 μl s^{-1} and a 0.25 mm of diameter needle. The cartridge heater temperature was set to 35 °C and a collector plate speed of 5 mm s^{-1} was employed for the printing.

The generation of both self-standing cylindric and square-shaped structures was evaluated for various aims. The tall cylinders of 6 mm in diameter and 4 cm height, composed of 200 layers, were printed with a plastic conical needle of 2 mm diameter. A light-curing printhead, operating at 365 nm with a fixed output power of 500 mW, was used to cure the sample after every 5 printed layers and for a duration of 40 s. For the generation of multilayer square models, a filled 0.6 cm^2 square-shaped layer with a 0.2 mm line spacing between fibers was printed using a stainless-steel needle with an inner diameter of 25 mm. 5 layers were printed and crosslinked for a duration of 40 s using the same UV light source. The printed gels were immersed in 300 μl of distilled water and incubated at 4 °C overnight to remove the sacrificial Pluronic 127 material from the structure. Subsequently, samples were washed with PBS (10 mM, pH 7.4) and re-equilibrated with SMC media prior to printing the cell-containing formulations on top.

For cell printing, inkjet dispensing using a valve-based printhead was employed. Specifically, a 0.1 mm diameter microvalve was employed for jetting with a dosing distance of 0.1 mm and valve opening and closing times of 700 μs and 300 μs, respectively. A printing height of 10 mm was used, printing 3 layers in the z-dimension, each composed of 10 lines (5 in each x and y dimension) of 6 mm in length, with a 1 mm spacing between lines, printed using a feed rate of 15 mm s^{-1}. The printing pressure was optimized for each cell containing formulation. In the case of the SMC bioink, a printing pressure of 0.050 MPa was applied, whilst for printing the endothelial cell suspension, a pressure of 0.035 Pa was employed. The SMC bioink was left to gel at 33 °C for 2 h before adding the corresponding cell media for cell culture. The following day, cell media was removed, and the endothelial cell suspension was printed on top of the SMC bioink. Once cells had adhered, cell media was added, and the systems were cultured at 33 °C. All the details of the printing parameters employed are described in Tables S6 and S7 (ESI†).

Arterial model characterisation

Cell growth and characterisation. The multi-layered printed constructs were incubated at 33 °C and 5% CO$_2$ in a humidified incubator, replacing cell media every 2–3 days. A stereoscope was used to observe changes in cell deposition over time. In

9440 | *J. Mater. Chem. B*, 2023, **11**, 9431–9442

This journal is © The Royal Society of Chemistry 2023

order to achieve higher resolution and differentiate between the two cell types using the CellTracker labels, fluorescence confocal imaging of the samples was conducted. Considering that our Zeiss 880 LSM microscope is inverted, the samples were flipped over prior to imaging. Live imaging was conducted using 405 nm (endothelial cells, stained with CellTracker Blue) and 633 nm (SMC, stained with CellTracker Deep Red) laser excitation. For nuclear and actin staining, samples were fixed (using 4% PFA) at various timepoints and stained using DAPI (1/500) and Actin 488 ReadyProbe (1/60 dilution) at 4 °C overnight. Images were process with ZEN and ImageJ software.

Biocompatibility. The biocompatibility of thermoresponsive gel was verified by incubating at 33 °C the 0.5 mM gel in sample tubes containing 500 μl cell media for 24 h, 48 h, and 5 days. All timepoints were calculated to finish at the same time. SMC and endothelial cells were thus plated the previous day at 1×10^4 cells per ml, 100 μl per well, in 96-well plates. The gel-incubated cell media was collected and 100 μl added to adhered cells in the 96 well plate. Cells were incubated at 33 °C for 24 h, followed by the LDH cell viability test to determine cell viability. For the LDH test, 50 μl of cell supernatant was transferred to a second 96-well plate and 50 μl of LDH reagent added. Controls included maximum LDH release (10% v/v lysis buffer resulting in total cell death), and spontaneous LDH release (non-treated cells). After 30 min, 50 μl of STOP solution was added and the absorbance at 490 and 680 nm was read.

RNA extraction and quantitative real time-qPCR (qPCR). Cells were recovered from the thermoresponsive multilayered cell-containing constructs using the Matrigel cell recovery solution. To do so, cell media was removed, and samples incubated in 300 μl of solution for 30 minutes at 4 °C, after which the depolymerization of the Matrigel was completed by pipetting. Cell containing material was pelleted at 1.4 kRPM for 5 minutes and subsequently frozen until their use for qRT-PCR analysis. The total RNA was extracted from cells using the RNeasy Mini Kit. The RNA was then reverse transcribed using a High-Capacity cDNA Reverse Transcription Kit, according to the manufacturer's instructions. The cDNA reverse transcription product was amplified with specific primers (Table S8, ESI†) by qPCR using the SYBR Green method with the kit iTaqTM Universal SYBR Green Supermix. The reaction was performed in triplicate on a CFX ConnectTM Real time PCR system. Relative normalized quantities (NRQ) of mRNA expression were calculated using the comparative Ct method (2-ΔΔCt). GAPDH was used as endogenous control and each gene was relativized to the expression of this housekeeping gene. Data was analysed using one-way ANOVA followed by Dunnett's Multiple Comparisons test) tested against Expanded Control ($*P \leq 0.05$, $**P \leq 0.01$, $***P \leq 0.001$, $****P \leq 0.0001$).

Author contributions

The manuscript was written through contributions of all authors. All authors have given approval to the final version of the manuscript.

Conflicts of interest

There are no conflicts to declare.

References

1 G. A. Roth, *et al.*, *J. Am. Coll. Cardiol.*, 2020, **76**, 2982–3021.
2 P. J. Barnes, S. Bonini, W. Seeger, M. G. Belvisi, B. Ward and A. Holmes, *Eur. Respir. J.*, 2015, **45**, 1197–1207.
3 P. M. Conn, *Animal models for the study of human disease*, Elsevier B.V., Oregon, USA, 2013.
4 A. J. Miller and J. R. Spence, *Physiology*, 2017, **32**, 246–260.
5 F. Martínez-Mardones, F. Fernandez-Llimos, S. I. Benrimoj, A. Ahumada-Canale, J. C. Plaza-Plaza, F. S. Tonin and V. Garcia-Cardenas, *J. Am. Heart Assoc.*, 2019, **8**, e013627.
6 H. Zhang, R. D. Whalley, A. M. Ferreira and K. Dalgarno, *Prog. Biomed. Eng.*, 2020, **2**, 022001.
7 E. Maestri, *BioTech*, 2021, **10**, 1–11.
8 Animals used for scientific purposes - Environment - European Commission, **https://ec.europa.eu/environment/chemicals/lab_animals/3r/alternative_en.htm**, (accessed 20 March 2023).
9 M. Kapałczyńska, T. Kolenda, W. Przybyła, M. Zajączkowska, A. Teresiak, V. Filas, M. Ibbs, R. Bliźniak, Ł. Łuczewski and K. Lamperska, *Arch. Med. Sci.*, 2018, **14**, 910.
10 S. V. Murphy and A. Atala, *Nat. Biotechnol.*, 2014, **32**, 773–785.
11 N. Noor, A. Shapira, R. Edri, I. Gal, L. Wertheim and T. Dvir, *Adv. Sci.*, 2019, **6**, 1900344.
12 T. Jiang, J. G. Munguia-Lopez, S. Flores-Torres, J. Kort-Mascort and J. M. Kinsella, *Appl. Phys. Rev.*, 2019, **6**, 011310.
13 Q. Zhang, N. Willis-Fox, C. Conboy and R. Daly, *Mater. Horizons*, 2021, **8**, 179–186.
14 R. Suntornnond, W. L. Ng, X. Huang, C. H. E. Yeow and W. Y. Yeong, *J. Mater. Chem. B*, 2022, **10**, 5989–6000.

This journal is © The Royal Society of Chemistry 2023

J. Mater. Chem. B, 2023, **11**, 9431–9442 | **9441**

15 G. Größbacher, M. Bartolf-Kopp, C. Gergely, P. N. Bernal, S. Florczak, M. de Ruijter, N. G. Rodriguez, J. Groll, J. Malda, T. Jungst and R. Levato, *Adv. Mater.*, 2023, 2300756.

16 F. Potere, B. Belgio, G. A. Croci, S. Tabano, P. Petrini, G. Dubini, F. Boschetti and S. Mantero, *Front. Bioeng. Biotechnol.*, 2022, **10**, 1465.

17 Q. Gao, Z. Liu, Z. Lin, J. Qiu, Y. Liu, A. Liu, Y. Wang, M. Xiang, B. Chen, J. Fu and Y. He, *ACS Biomater. Sci. Eng.*, 2017, **3**, 399–408.

18 F. Martino, A. R. Perestrelo, V. Vinarský, S. Pagliari and G. Forte, *Front. Physiol.*, 2018, **9**, 824.

19 C. Hahn and M. A. Schwartz, *Nat. Rev. Mol. Cell Biol.*, 2009, **10**, 53–62.

20 D. B. Camasão and D. Mantovani, *Mater. Today Bio*, 2021, **10**, 100106.

21 O. V. Sazonova, K. L. Lee, B. C. Isenberg, C. B. Rich, M. A. Nugent and J. Y. Wong, *Biophys. J.*, 2011, **101**, 622–630.

22 R. Moreno-Vicente, D. M. Pavón, I. Martín-Padura, M. Catalá-Montoro, A. Díez-Sánchez, A. Quílez-Álvarez, J. A. López, M. Sánchez-Álvarez, J. Vázquez, R. Strippoli and M. A. del Pozo, *Cell Rep.*, 2018, **25**, 1622–1635.e6.

23 E. K. Paluch, C. M. Nelson, N. Biais, B. Fabry, J. Moeller, B. L. Pruitt, C. Wollnik, G. Kudryasheva, F. Rehfeldt and W. Federle, *BMC Biol.*, 2015, **13**, 1–14.

24 D. E. Jaalouk and J. Lammerding, *Nat. Rev. Mol. Cell Biol.*, 2009, **10**, 63–73.

25 W. M. Ciszewski, M. E. Wawro, I. Sacewicz-hofman and K. Sobierajska, *Int. J. Mol. Sci.*, 2021, **22**, 11607.

26 D. H. Kim, K. Han, K. Gupta, K. W. Kwon, K.-Y. Suh and A. Levchenko, *Biomaterials*, 2009, **30**, 5433–5444.

27 T. Panciera, L. Azzolin, M. Cordenonsi and S. Piccolo, *Nat. Rev. Mol. Cell Biol.*, 2017, **18**, 758–770.

28 G. Jia and J. R. Sowers, *Diabetes*, 2015, **64**, 3645.

29 M. J. Thubrikar and F. Robicsek, *Ann. Thorac. Surg.*, 1995, **59**, 1594–1603.

30 C. Pan, Q. Gao, B. S. Kim, Y. Han and G. Gao, *Micromachines*, 2022, **13**, 326.

31 Z. U. Arif, M. Y. Khalid, W. Ahmed and H. Arshad, *Bioprinting*, 2022, **27**, e00203.

32 R. R. Mechoor, T. Schmidt and E. Kung, *J. Biomech. Eng.*, 2016, **138**, 111002.

33 F. Doberenz, K. Zeng, C. Willems, K. Zhang and T. Groth, *J. Mater. Chem. B*, 2020, **8**, 607–628.

34 G. Baffou and R. Quidant, *Laser Photon. Rev.*, 2013, **7**, 171–187.

35 A. Espinosa, J. Kolosnjaj-Tabi, A. Abou-Hassan, A. Plan Sangnier, A. Curcio, A. K. A. Silva, R. Di Corato, S. Neveu, T. Pellegrino, L. M. Liz-Marzán and C. Wilhelm, *Adv. Funct. Mater.*, 2018, **28**, 1803660.

36 M. Moros, A. Lewinska, F. Merola, P. Ferraro, M. Wnuk, A. Tino and C. Tortiglione, *ACS Appl. Mater. Interfaces*, 2020, **12**, 13718–13730.

37 K. Jiang, D. A. Smith and A. Pinchuk, *J. Phys. Chem. C*, 2013, **117**, 27073–27080.

38 L. Scarabelli, A. Sánchez-Iglesias, J. Pérez-Juste and L. M. Liz-Marzán, *J. Phys. Chem. Lett.*, 2015, **6**, 4270–4279.

39 E. Lenzi, D. Jimenez de Aberasturi and L. M. Liz-Marzán, *ACS Sens.*, 2019, **4**, 1126–1137.

40 J. Reguera, J. Langer, D. Jimenez de Aberasturi and L. M. Liz-Marzán, *Chem. Soc. Rev.*, 2017, **46**, 3866–3885.

41 H. G. Schild, *Prog. Polym. Sci.*, 1992, **17**, 163–249.

42 K. H. Son and J. W. Lee, *Materials*, 2016, **9**, 854.

43 C. García-Astrain, E. Lenzi, D. Jimenez de Aberasturi, M. Henriksen-Lacey, M. R. Binelli and L. M. Liz-Marzán, *Adv. Funct. Mater.*, 2020, **30**, 2005407.

44 K. R. Pulagam, M. Henriksen-Lacey, K. B. Uribe, C. Renero-Lecuna, J. Kumar, A. Charalampopoulou, A. Facoetti, N. Protti, V. Gómez-Vallejo, Z. Baz, V. Kumar, A. Sánchez-Iglesias, S. Altieri, U. Cossío, D. Di Silvio, A. M. Martínez-Villacorta, A. Ruiz De Angulo, L. Rejc, L. M. Liz-Marzán and J. Llop, *ACS Appl. Mater. Interfaces*, 2021, **13**, 49589–49601.

45 N. Mathern, E. Yousefian, H. Ridwan, O. Nikoubashman and M. Wiesmann, *PLoS One*, 2022, **17**, e0268005.

46 M. García-García, S. Sánchez-Perales, P. Jarabo, E. Calvo, T. Huyton, L. Fu, S. C. Ng, L. Sotodosos-Alonso, J. Vázquez, S. Casas-Tintó, D. Görlich, A. Echarri and M. A. Del Pozo, *Nat. Commun.*, 2022, **13**, 1–21.

47 A. Alave Reyes-Furrer, S. De Andrade, D. Bachmann, H. Jeker, M. Steinmann, N. Accart, A. Dunbar, M. Rausch, E. Bono, M. Rimann and H. Keller, *Commun. Biol.*, 2021, **4**, 1–12.

48 X. Li, P. Tsai, E. D. Wieder, A. Kribben, V. Van Putten, R. W. Schrier and R. A. Nemenoff, *J. Biol. Chem.*, 1994, **269**, 19653–19658.

49 N. T. Kohen, L. E. Little and K. E. Healy, *Biointerphases*, 2009, **4**, 69–79.

50 S. Islam, K. I. Boström, D. Di Carlo, C. A. Simmons, Y. Tintut, Y. Yao and J. J. Hsu, *Front. Physiol.*, 2021, **12**, 734215.

51 K. Balachandran, P. W. Alford, J. Wylie-Sears, J. A. Goss, A. Grosberg, J. Bischoff, E. Aikawa, R. A. Levine and K. K. Parker, *Proc. Natl. Acad. Sci. U. S. A.*, 2011, **108**, 19943–19948.

52 G. Krenning, V. G. Barauna, J. E. Krieger, M. C. Harmsen and J. R. A. J. Moonen, *Stem Cells Int.*, 2016, **5**, 15.

53 E. E. Bastounis, Y. T. Yeh and J. A. Theriot, *Sci. Rep.*, 2019, **9**, 1–16.

54 S. J. Lue, C.-H. Chen and C.-M. Shih, *J. Macromol. Sci., Part B: Phys.*, 2011, **50**, 563–579.

55 L. Scarabelli, M. Grzelczak and L. M. Liz-Marzán, *Chem. Mater.*, 2013, **25**, 4232–4238.

56 FMRIB Analysis Group, "FSL – FslWiki," can be found under **https://fsl.fmrib.ox.ac.uk/fsl/fslwiki/**, 2012.

57 C3D.ORG – C3D applications, **https://www.c3d.org/c3dapps.html**.

58 P. A. Yushkevich, J. Piven, H. C. Hazlett, R. G. Smith, S. Ho, J. C. Gee and G. Gerig, *NeuroImage*, 2006, **31**, 1116–1128.

59 ITK-SNAP Home, can be found under **http://www.itksnap.org/pmwiki/pmwiki.php**, 2014.